Magnetic and Structural Phase Transitions in the Spinel Compound $Fe_{1+x}Cr_{2-x}O_4$

J. Ma,[1] V. O. Garlea,[1] A. Rondinone,[2] A. A. Aczel,[1] S. Calder,[1] C. dela Cruz,[1] R. Sinclair,[3] W. Tian,[1] Songxue Chi,[1] A. Kiswandhi,[4,5] J. S. Brooks,[4,5] H. D. Zhou,[3,4] and M. Matsuda[1]

[1] *Quantum Condensed Matter Division, Oak Ridge National Laboratory, Oak Ridge, TN 37831, USA*
[2] *Center for Nanophase Materials Sciences, Oak Ridge National Laboratory, Oak Ridge, TN 37831, USA*
[3] *Department of Physics and Astronomy, University of Tennessee, Knoxville, TN 37996, USA*
[4] *National High Magnetic Field Laboratory, Florida State University, Tallahassee, FL 32306, USA*
[5] *Department of Physics, Florida State University, Tallahassee, FL 32306-3016, USA*

(Dated: February 28, 2022)

Neutron and X-ray diffraction, magnetic susceptibility, and specific heat measurements have been used to investigate the magnetic and structural phase transitions of the spinel system $Fe_{1+x}Cr_{2-x}O_4$ ($0.0 \leq x \leq 1.0$). The temperature versus Fe concentration (x) phase diagram features two magnetically ordered states and four structural states below 420 K. The complexity of the phase diagram is closely related to the change in the spin and orbital degrees of freedom induced by substitution of Fe ions for Cr ions. The systematic change in the crystal structure is explained by the combined effects of Jahn-Teller distortion, spin-lattice interaction, Fe^{2+}-Fe^{3+} hopping, and disorder among Fe^{2+}, Fe^{3+}, and Cr^{3+} ions.

PACS numbers: 61.05.fm, 75.25.Dk, 75.30.Cr, 75.40.Cx, 75.47.Lx

I. INTRODUCTION

Due to the strong interactions among the spin, orbital, and lattice degrees of freedom, the transition metal oxides with spinel structure, AB_2O_4, present complicated magnetic and structural phase transitions and have attracted extensive attention in past years.[1–3] In the system, the octahedrally coordinated B-site cations form a geometrically frustrated network of corner shared tetrahedra, while the A-site cations form a diamond lattice and are located at the center of oxygen-tetrahedra. The $3d$ orbitals of the B-site cation split into the triply degenerate low-energy t_{2g} states and doubly degenerate high-energy e_g states, while the A-site cation has two low energy e_g states with three high energy t_{2g} states.[3,4] Since the properties of both A and B cations are driven by the electron occupancies on $3d$ orbitals, which determine the magnetic and orbital degrees of freedom, it is challenging to obtain the original driving forces for those magnetic and structural phase transitions in the spinel oxides.

In order to get insightful information on the phase transition mechanism, one can occupy the B^{3+}-site with a spin only cation, (such as the chromite spinels ACr_2O_4). The electronic configuration for Cr^{3+} cation is $3d^3(S(Cr^{3+})=3/2)$, which leads to half filled t_{2g} and empty e_g orbitals. In addition, it has been found that different A-site cations could yield different ordered states: i) If A^{2+} ions are magnetically neutral, such as $ZnCr_2O_4$,[1,5–8] $MgCr_2O_4$,[7–9] $CdCr_2O_4$,[8,10] and $HgCr_2O_4$,[8,11,12] a transition from the paramagnetic cubic phase to the Néel-ordered tetragonal or orthorhombic one at low temperatures is obtained. ii) If A^{2+} ions are magnetic with spin only, such as $MnCr_2O_4$ ($S(Mn^{2+})=5/2$),[13–17] and $CoCr_2O_4$($S(Co^{2+})=3/2$),[13–21] the lattice remains cubic, with a paramagnetic-to-ferrimagnetic transition at high temperature, followed by a transition to spiral ordering at lower temperature due to weak magnetic geometrical frustration. iii) If A^{2+} ions are magnetic with the orbital degree of freedom, such as $FeCr_2O_4$,[17,20–25] $NiCr_2O_4$,[17,21–23,26,27] and $CuCr_2O_4$,[17,21,22,27–29] a cubic-tetragonal phase transition is observed at a higher temperature, followed by magnetic order, which indicates that the magnetic ordering is stabilized by reducing the lattice symmetry through a spin-lattice coupling. The long-range ordered collinear ferrimagnetic state can eventually evolve into different noncollinear ferrimagnetic states at a lower temperature, such as conical ordering in $FeCr_2O_4$ and $NiCr_2O_4$, and Yafet-Kittel-type magnetic ordering in $CuCr_2O_4$. Moreover, the multiferroic ordering and the dielectric response induced by the magnetic field also have been found in several chromium spinel oxides.[17,20–22,30,31] Substantial experimental and theoretical works have been performed to study the intriguing properties of ACr_2O_4. Previously, a largely separate line of research has been devoted to the spin-lattice interaction which is related to the spin frustration and the cooperative Jahn-Teller distortion especially for the compounds involving orbitally active A-site cations.[17,20–22,27,31–35] However, very few materials have been studied from the view point of the coupling between frustration and Jahn-Teller effects by changing the orbital configuration of B-site cation.

In this regard, $Fe_{1+x}Cr_{2-x}O_4$ is a remarkable compound. The Fe^{3+} ions ($3d^5$) are not orbitally active and have a large spin, $S = 5/2$, while Fe^{2+} ions have an orbital degree of freedom with $3d^6$ and $S = 2$. Since the Cr^{2+} energy level lies well above the $Fe^{2+/3+}$ energy levels, the valence of Cr^{3+} is stable. Although electrons have been reported to be hopping between A- and B-sites for $x \geq \sim 0.8$,[36,37] the Cr^{3+} ions always stay at the B-site and the only electron transfer should be between Fe^{2+} and Fe^{3+} ions. This arrangement leads to the $3d$ electronic ground state of Fe^{2+} ion changing from e_g on the A-site to t_{2g} on the B-site and the type of the Jahn-Teller distortion

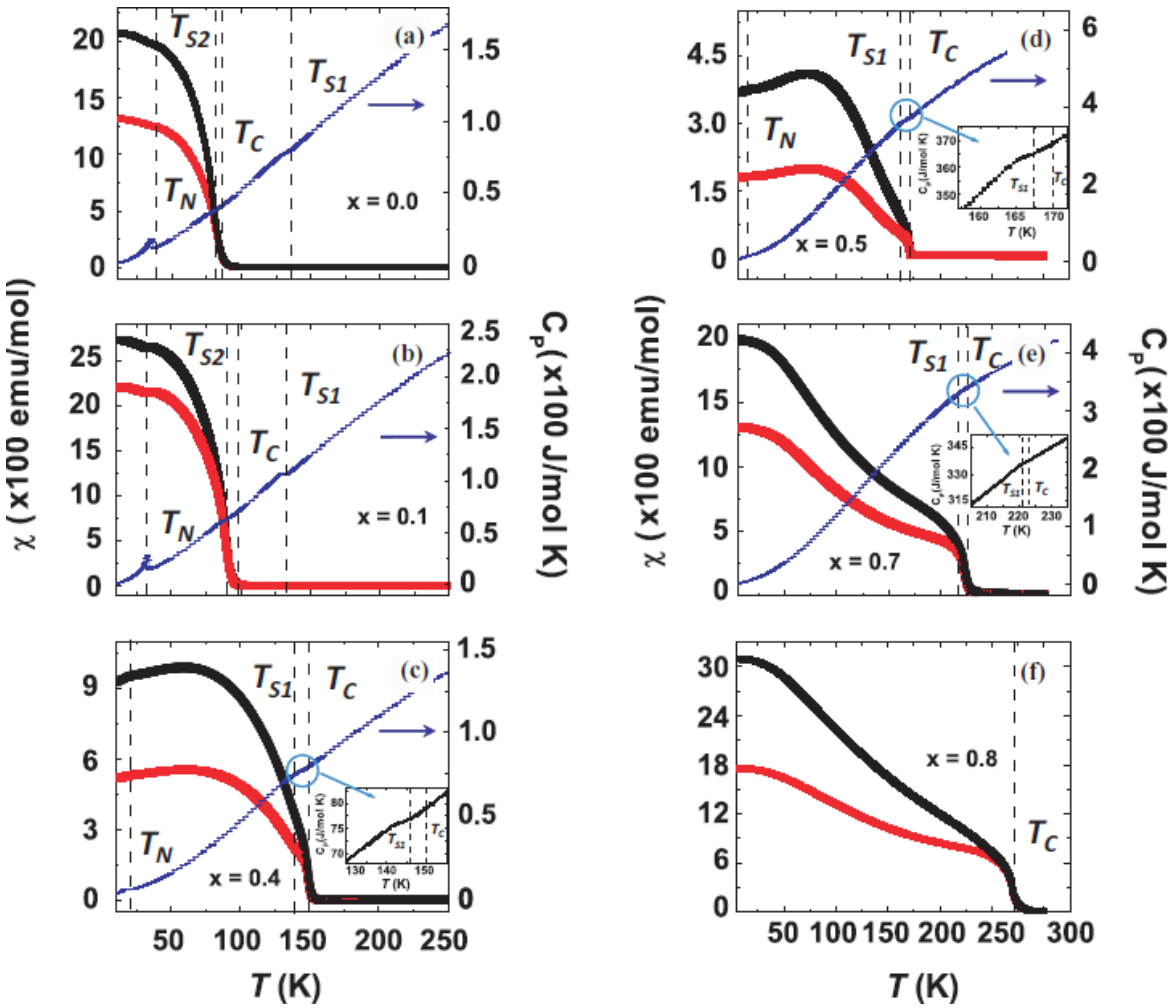

FIG. 1. (Color online) The temperature dependence of magnetic susceptibilities and specific heat for $Fe_{1+x}Cr_{2-x}O_4$ ($0.0 \leq x \leq 0.8$). Black and red lines are the results of the field-cooled(FC) and zero-field-cooled(ZFC) measurements, respectively. The blue line presents the specific heat data. For $x \leq 0.3$, T_{S_2} is close to T_C; For $0.3 \leq x \leq 0.8$, T_{S_1} is close to T_C. Insets present the enlarged view of the specific heat data around T_{S_1} and T_C.

effect being alternated in the system.[37–40] Therefore, the primary effect of Fe-doping in this system is to change the average moment on the B-sites and alter the competition of antiferromagnetic interactions between A-B and B-B. For this reason, studying the magnetic and structural lattice of $Fe_{1+x}Cr_{2-x}O_4$ can help to uncover the origin of the orbital ordering effect on the structural transition.

The structure was first discussed by Verwey et al. in 1947,[38] then several techniques had been applied to study the physical properties. In 1964, G. Shirane et al.[25] measured the magnetic structures of the parent compound $FeCr_2O_4$ by neutron powder diffraction (NPD). In 2008, Tomiyasu et al.[23] reported the dynamical spin-frustration effect on the magnetic excitations of $FeCr_2O_4$. Both composition and temperature dependences of cubic-tetragonal-orthorhombic structure transitions had been reported by X-ray powder diffraction (XPD) and specific heat.[37,39–43] The magnetic properties had been studied by magnetic and Mössbauer effect measurements.[36,42–45] However, a systematic study of the doping effect on magnetic structures is still missing, and the T-x phase diagram is still under debate.[41,42]

In this paper, the magnetic and crystal structure of $Fe_{1+x}Cr_{2-x}O_4$ ($0.2 \leq x \leq 1.0$) are studied by NPD, XPD, magnetic susceptibility, and specific heat measurements. The phase diagram for $0.0 \leq x \leq 1.0$ is also constructed. The measurements confirm the existence of a paramagnetic-to-collinear ferrimagnetic phase transition for the entire x range and a conical ferrimagnetic state at low temperature in the low Fe-doping region ($x \leq 0.6$). The structural phase transition is complicated: Although the cubic-to-tetragonal transition ($0.0 \leq x \leq 0.8$) and a short-range tetragonal distortion is suggested ($0.8 \leq x \leq 1.0$), the related structural transition temperature (T_{S_1}) decreases at $x \leq 0.3$, then increases gradually

at $0.3 \leq x \leq 0.8$, and decreases again at $x \geq 0.8$. In addition, a tetragonal-to-orthorhombic transition is detected at T_{S_2} and disappears at the high Fe-doping region ($x \geq 0.7$). We extend the study of phase diagram to compositions beyond 0.4 and temperatures below 80 K. These observations not only emphasize the competitions among the spin-lattice interaction, the Jahn-Teller distortion, the cooperative spin-orbital coupling, and the disordered states of the A- and B-site ions, but also reveal the effect of the magnetic moment magnitude and electron hopping on this frustrated spinel system.

II. EXPERIMENT

Polycrystalline samples of $Fe_{1+x}Cr_{2-x}O_4$ ($0 \leq x \leq 1.0$) were synthesized by solid state reaction. Stoichiometric mixtures of Fe_2O_3, Fe, and Cr_2O_3 were ground together and calcined under flowing Ar at 1150°C for 20 h. The magnetic susceptibility was measured with a SQUID (Quantum Design) with an applied field H = 100 Oe with zero field(ZFC) and field cooling processes(FC). The specific heat measurements were performed on a Quantum Design physical property measurement system (PPMS).

Low-temperature XPD patterns were collected using a PANalytical Multi-Purpose Diffractometer (MPD) equipped with an Oxford Cryosystems PheniX cryostage closed-cycle helium refrigerator. The MPD was configured with copper $K_{\alpha_{1,2}}$ radiation and fixed slits, a diffracted-beam monochromator to minimize background fluorescence from iron, and a high-speed X'celerator position-sensitive detector. The powder samples were either pressed in a stainless-steel cup or solution-cast from ethanol onto an anodized flat holder, depending on the amount of material available. The instrument alignment was verified prior to the data collection using NIST 660a LaB_6 standard, but no internal standards were used in order to prevent contamination of the samples. The cryostage was operated under a vacuum of approximately 10^{-6} Torr. Data were collected over broad and limited diffraction angles in order to verify structure and to carefully examine the structural transitions over a broad temperature range from 15 to 300 K. The X'Pert HighScore Plus software was employed to identify possible phases and determine the lattice parameters.

NPD experiments were performed at the High Flux Isotope Reactor (HFIR) of the Oak Ridge National Laboratory (ORNL). For each composition, about 5 g of powder was loaded in a vanadium-cylinder can. A closed-cycle refrigerator was employed for samples with $x \leq 0.8$, while a cryofurnace was used for samples with $0.9 \leq x \leq 1.0$. Preliminary neutron diffraction data were obtained from the Wide Angle Neutron Diffractometer (WAND). High-resolution neutron powder diffraction measurements were performed using the neutron powder diffractometer, HB2A. Data were collected at selected temperatures using two different wavelengths λ =1.538 and 2.406 Å and collimation of 12'-open-6'. The shorter wavelength gives a greater intensity and higher Q coverage that was used to investigate the crystal structures in this low temperature regime, while the longer wavelength gives lower Q coverage with better resolution that was important for investigating the magnetic structures of the material. The diffraction data were analyzed using the Rietveld refinement program FullProf.[46]

The magnetic order parameter measurements were carried out using the HB1A triple-axis spectrometer at HFIR. HB1A was operated with an incident neutron wavelength of λ = 2.359 Å. A pyrolytic graphite (PG) (002) monochromator and analyzer were used together with collimation of 40′-40′-40′-80′. Contamination from higher-order beams was removed using PG filters.

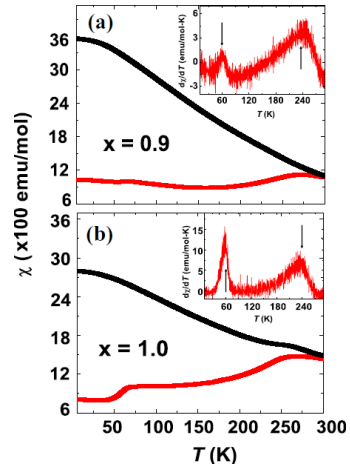

FIG. 2. (Color online) The temperature dependence of magnetic susceptibilities for $Fe_{1+x}Cr_{2-x}O_4$ (x = 0.9(a) and 1.0(b)). Black and red lines are the results of FC and ZFC measurements, respectively. The insets are the related temperature derivative of the ZFC susceptibilities and the arrows mark the peak positions in temperature.

III. RESULTS

A. Magnetic Susceptibility and Specific Heat

Figure 1 shows the temperature dependence of magnetic susceptibilities for $Fe_{1+x}Cr_{2-x}O_4$ ($0.0 \leq x \leq 0.8$). As the temperature decreases, the curves of ZFC and FC split at the paramagnetic-to-ferrimagnetic transition temperature, T_C, and an additional magnetic phase transition becomes apparent at low temperature, T_N, for the low Fe-doped compounds ($x \geq 0.6$). The composition dependent T_C agree with the previous reports.[36,42,43] As Fe content increases, T_C increases gradually. For the second magnetic phase transition temperature, T_N, it decreases with more Fe^{3+} ions introduced to the B-site. As described in the following section, this transition corresponds to a spin reorientation into a noncollinear conical state.

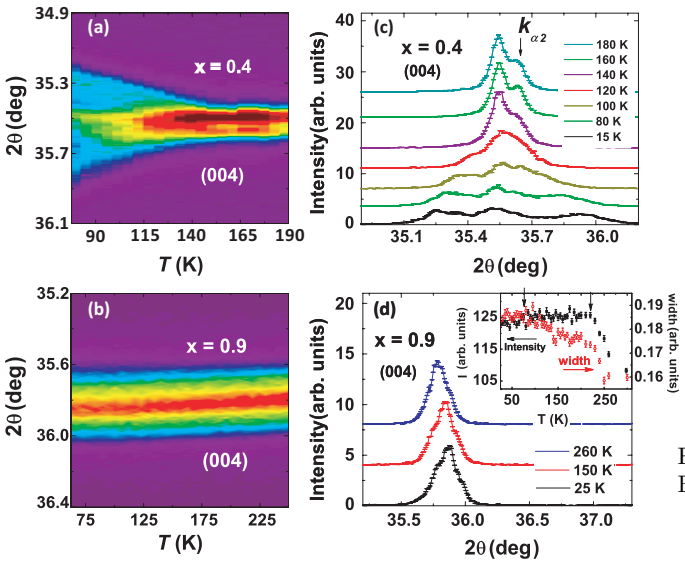

FIG. 3. (Color online) The 2θ dependence of the (004) Bragg peak of $Fe_{1+x}Cr_{2-x}O_4$ ($x = 0.4$(a) and 0.9(b)) as a function of temperature by XPD. The XPD data around the cubic (004) Bragg position of $x = 0.4$(c) and 0.9(d) at selected temperatures. Inset shows the width(open circle) and integrated intensity(filled square) of the (004) Bragg reflections of $x = 0.9$ by XPD.

For the high Fe-doped compounds ($x \geq 0.9$), T_C is above room temperature, as shown in Fig. 2. Although there is no obvious anomaly observed from the FC data, there are two peaks obtained from the temperature derivative of the ZFC susceptibility, which might be related to Jahn-Teller effects from the non-degenerate e_g and t_{2g}orbitals and will be discussed in the following sections.

In order to check the effect of the magnetic transitions on the lattice, the specific heat was measured from 2 to 300 K for several compounds, such as $x = 0.0$, 0.1, 0.4, 0.5, and 0.7, as shown in Fig. 1(a) – (e). For $x \leq 0.4$, the structural transition temperatures are comparable to the data of Kose et al..[42] The apparent structural transition becomes less distinct with Fe-doping. In addition, the data of specific heat clearly present the collinear-to-noncollinear ferrimagnetic transition for $x \leq 0.6$. Therefore, there are two distinct structural transitions for the low Fe concentration ($x \leq 0.3$). One is observed in the paramagnetic state, above T_C, and the other emerges in the vicinity of the magnetic ordering temperature. Those structural transitions are also in agreement with the diffraction data, which we will discuss the details in the following sections.

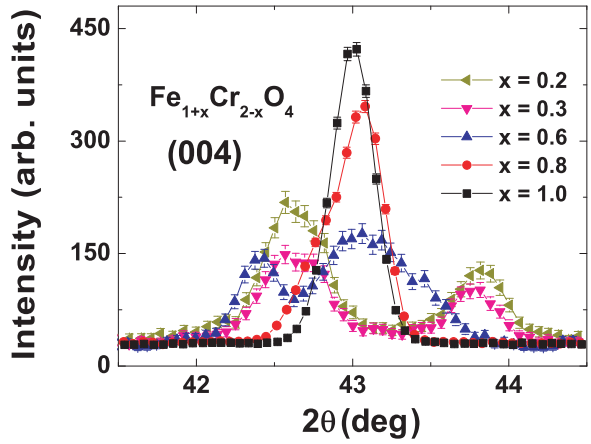

FIG. 4. (Color online) The NPD data around the cubic (004) Bragg position for different compositions at 5 K

.

B. Neutron and X-ray diffraction

The structural and magnetic phases of $Fe_{1+x}Cr_{2-x}O_4$ system are identified by NPD and XPD on several different compositions. The temperature dependences of the (004) Bragg peak intensity of $Fe_{1+x}Cr_{2-x}O_4$ (x=0.4 and 0.9) measured by XPD are plotted in Fig. 3.

For the low Fe-doped compound, such as $x = 0.4$, the structure changes from cubic to tetragonal at $T_{S_1} \sim 150$ K and then to orthorhombic at $T_{S_2} \sim 110$ K, as shown in Fig. 3(a); For the high Fe-doped compound, such as $x = 0.9$, there is no obvious structural phase transition observed and the symmetry is cubic, as shown in Fig. 3(b). The composition dependence of the diffraction pattern observed at 5 K is shown in Fig. 4. The three different patterns were well described by the space groups $Fd\bar{3}m$ (one peak), $I41/amd$ (two peaks), and $Fddd$ (three peaks). This is consistent with the previous analysis and reflecting the cubic-tetragonal-orthorhombic sequence of structural phase transitions upon decreasing the Fe amount.[37,39–43] Because of the limited instrumental resolution, the two peaks of the tetragonal phase ($x = 0.8$) are observed as one broad peak, and two peaks (one is sharp and the other is broad) are observed in the orthorhombic phase instead of three sharp peaks for $x = 0.2, 0.3$ and 0.6, Fig. 4. For the high Fe-doped compound ($x \geq 0.9$), although the phase transition related peak splitting is not fully perceived with the current XPD experimental resolution, the peak widths of (004) at 20 K are broader than at 300 K. The two characteristic temperatures indicated by the magnetic susceptibility measurements are marked by arrows shown in Fig. 3(d). The temperature dependent anomaly at $\sim$ 210K is strong on both integrated intensities and peak widths, hence a tetragonal phase is suggested, which agrees with Francombe et al..[43] On the other hand, there is no apparent anomaly at $\sim$ 60 K. It is possible that the anomalies in the magnetic susceptibilities originate from the transi-

TABLE I. Crystallographic information and Rietveld profile reliability factors for $Fe_{1+x}Cr_{2-x}O_4$ (x=0.2, 0.3, 0.6, 0.8, and 1.0) from NPD data at 5 K.

	$x = 0.2$	$x = 0.3$	$x = 0.6$	$x = 0.8$	$x = 1.0$
Crystal symmetry	orthorhombic	orthorhombic	orthorhombic	tetragonal	cubic
Space group	$Fddd$	$Fddd$	$Fddd$	$I41/amd$	$Fd\bar{3}m$
a (Å)	8.4300(4)	8.4294(4)	8.3945(5)	5.9179(1)	8.3792(1)
b (Å)	8.4710(3)	8.4754(4)	8.4919(4)	–	–
c (Å)	8.2343(3)	8.2414(5)	8.3172(5)	8.4193(1)	–
c/a	0.977	0.978	0.991	1.001	1.000
V ($Å^3$)	588.0(1)	588.8(1)	592.9(1)	294.86(1)	588.32(1)
Z	8	8	8	8	4
Recording angular range(°)	10.5–131.9	10.5–131.9	10.5–131.9	10.5–131.9	10.5–131.9
calculated density (g/cm^3)	5.074	5.068	5.067	5.110	5.142
Bragg R-factor	11.5	8.5	5.7	5.5	5.6
Magnetic R-factor	11.1	8.2	6.9	6.8	4.2

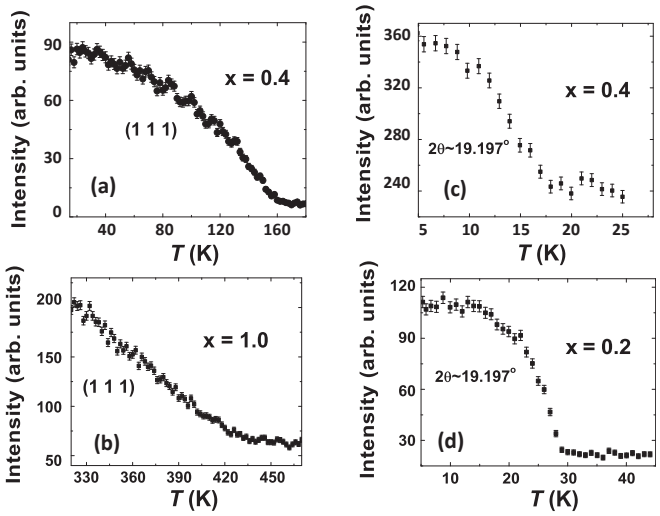

FIG. 5. (Color online) The neutron diffraction data of $Fe_{1+x}Cr_{2-x}O_4$ upon warming. The paramagnetic-to-collinear ferrimagnetic transitions of $x = 0.4$ (a) and 1.0 (b) are presented by the integrated intensities of (111) Bragg peaks, and the integrated intensities of the incommensurate reflection at 19.197° presents the collinear-to-conical ferrimagnetic transitions of $x = 0.4$ (c) and 0.2(d), respectively.

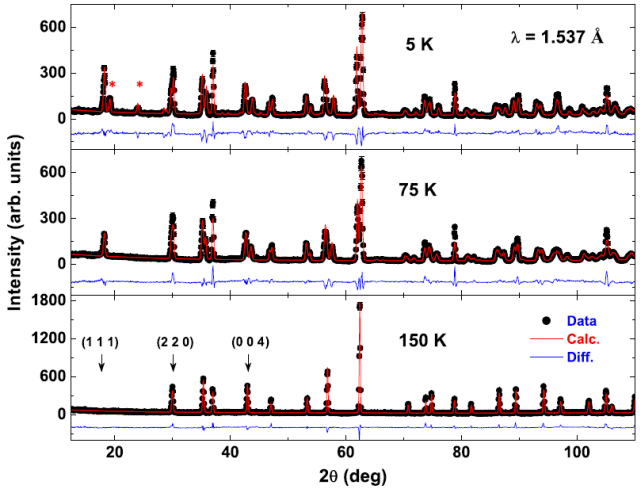

FIG. 6. (Color online) Plots of raw NPD data (black dots) for $Fe_{1.2}Cr_{1.8}O_4$ measured at $T = 5$, 75, and 150 K for $2\theta \leq 120°$. Solid lines are results of Rietveld refinements described in the main text. Differences between observed and calculated intensities are shown directly below the respective patterns. The stars indicate an incommensurate phase.

tion/crossover to the different ground state of e_g orbitals due to the structural transition/distortion. Therefore, we speculate that the anomaly at $\sim$ 60 K is also related with a structural distortion. Due to the instrumental resolution, the difference between a structural distortion and a structural transition cannot be fully resolved, i.e. a change that is observed as a peak broadening rather than a distinct peak splitting. So far, we cannot confirm the new phase around 60 K with lab XPD. Synchrotron or single crystal diffraction could make it possible to investigate the structural transitions/distortions more accurately, however, this is beyond the scope of the current investigations.

Fig. 5 presents the order parameters of the (111) and incommensurate satellite reflections measured by NPD for different Fe concentrations. The rise of the (111) magnetic Bragg intensities indicate a collinear ferrimagnetic order set in at $\sim$ 150 K ($x = 0.4$) and $\sim$ 410 K ($x = 1.0$), respectively, which are in a good agreement with the previous reports[36,41–43] and the bulk magnetization well for $x = 0.4$, as shown in Fig. 1. Similar to the parent compound, $FeCr_2O_4$,[25] the collinear-to-noncollinear ferrimagnetic transitions are also observed by the appearance of incommensurate magnetic reflections at T_N, which are $\sim$ 28 K for $x = 0.2$ and $\sim$ 18 K for $x = 0.4$, respectively. Actually, this incommensurate peaks have also been reported in other magnetic A-site chromites, such as $CuCr_2O_4$, $MnCr_2O_4$ and $CoCr_2O_4$.[13–15,18,19,34]

Rietveld analyses were employed to determine precisely the changes in both the crystal and magnetic structures for each composition. The Rietveld fitted patterns on $Fe_{1.2}Cr_{1.8}O_4$ at 150, 75, and 5 K are shown in Fig. 6. Figure 7 displays the Rietveld profile fitting results at 5

K for selected Fe compositions. The data at 150 K for $Fe_{1.2}Cr_{1.8}O_4$ confirm the cubic spinel structure(defined by $Fd\bar{3}m$ space group) without impurity phases. The refinement results indicate that less than 0.5% dislocations between A- and B-site in $Fe_{1.2}Cr_{1.8}O_4$, which confirms the statement of the Cr^{2+} energy level lying well above the $Fe^{2+/3+}$ energy level.[37,39] Similar to FeV_2O_4,[47] the diffraction patterns are well described by the space groups $Fd\bar{3}m$ for the cubic lattice and the $Fddd$ for orthorhombic lattice with decreasing temperature, while the magnetic phases are well described by the collinear and conical magnetic states, respectively. The conical magnetic phase is an incommensurate phase (with the corresponding reflections labeled by stars in Fig. 6(a) and Fig. 7(a)). Upon Fe-doping, the positions of incommensurate peaks do not change significantly, but the intensities decrease. In order to model these reflections, we have tried the conical model with ferrimagnetic order along [110] (as in $MnCr_2O_4$[13,14]) or along c-axis (as found for $CuCr_2O_4$[28]). The quality of the fits is not very satisfactory for either model, being affected by an anisotropic peak broadening which may be results from the peak broadening which might come from the microstrains or other structural distortions in the sample. One the other hand, the lack of enough unique magnetic peaks in this powder data hinders the reliable determination of the direction and magnitude of the Fe^{2+} and Fe^{3+}/Cr^{3+} magnetic moments. Single crystal neutron diffraction measurements are clearly needed to determine the exact canting angles and ordered moments. Figs. 6(a) and 7(a) present the best fits from the refinements with the propagation vector of $k = [0.391, 0.391, 0]$ for the centered cell $Fddd$. Detailed information about the structural refinement and the atomic coordinates is summarized in Table I and II. The doping effect on the tetragonal splitting is also confirmed by the change of the c/a ratio.[25,37,39–43]

The cubic-tetragonal-orthorhombic sequence of structural phase transition is also captured by the XPD measurements with 5 K/ step, which is consistent with the previous analysis[42] and similar to other FeB_2O4 spinels, such as Mn-doped chromite $Fe_{1-x}Mn_xCr_2O_4$[34] and Fe-vanadate $Fe_{1+x}V_{2-x}O_4$.[47–49]

IV. DISCUSSION

Combining the diffraction and the magnetic susceptibility measurements, a $T-x$ phase diagram including both the crystal and magnetic structures can be constructed as shown in Fig. 8. The complicated phase diagram clearly presents the Fe^{3+}-doping effects on the Jahn-Teller distortion, spin-lattice interaction, orbital-lattice interaction, Fe^{2+}-Fe^{3+} hopping, and disordering effect of Fe^{2+}, Fe^{3+}, and Cr^{3+} ions in the system. There are three major regions, which will now be discussed separately.

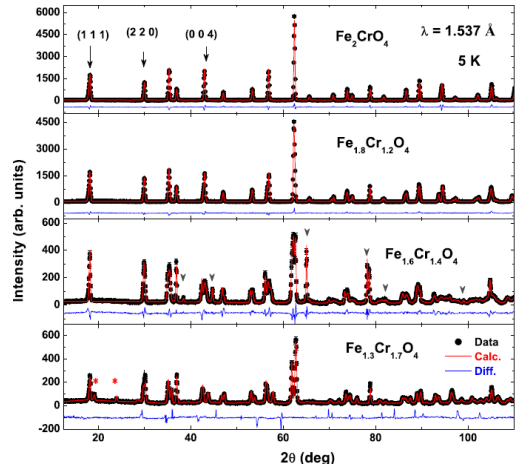

FIG. 7. (Color online) Plots of NPD data (black dots) for $Fe_{1+x}Cr_{2-x}O_4$($x = 0.3$, 0.6, 0.8, and 1.0) measured at $T = 5$ K for $2\theta \leq 120°$. Solid lines are results of Rietveld refinements described in the main text. Differences between observed and calculated intensities are shown below the respective patterns. The stars indicate an incommensurate phase and the grey arrows are the signal from Al-can.

i) $x \leq 0.3$,

The doped Fe^{3+} ions only occupy the B-site of the spinel, and the compounds have the normal type of structure with the formula $Fe^{2+}[Cr^{3+}_{2-x}Fe^{3+}_x]O_4$.[36,37,39–43,45] The paramagnetic-to-collinear ferrimagnetic and collinear-to-conical ferrimagnetic phase transitions are observed at T_C and T_N, respectively. With increasing Fe-doping, T_C increases and T_N decreases. Although the cubic, tetragonal, and orthorhombic phases are observed in sequence as temperature decreases, T_{S_1} decreases with Fe-doping while T_{S_2} increases with T_C. Moreover, the lattice constant a is larger than c in the related tetragonal phase.

The 6 outer-shell electrons of Fe^{2+} occupy the $3d$ orbitals ($e_g^3 t_{2g}^3$), giving one of the three e_g electrons the orbital degree of freedom on $3d_{z^2}$ or $3d_{x^2-y^2}$. Since the FeO_4 tetrahedra are generated from a cube where one Fe^{2+} ion is located at the center of four O^{2-} ions that occupy two diagonal corners, the distortion modes can be represented, as discussed in Ref. [34], by a combination of $3d_{z^2}$ and $3d_{x^2-y^2}$, which are described by Q_2 and Q_3, respectively,[34,50,51]

$$Q_2 = \frac{1}{\sqrt{2}L}(\delta X - \delta Y)\,,$$
$$Q_3 = \frac{1}{\sqrt{6}L}(2\delta Z - \delta X - \delta Y)\,, \quad (1)$$

where L is the length of the related cube, δX, δY, and δZ are the modulation of the cube dimensions.

Thus, the Hamiltonian of the coupling between the distortion and orbital occupation should be,

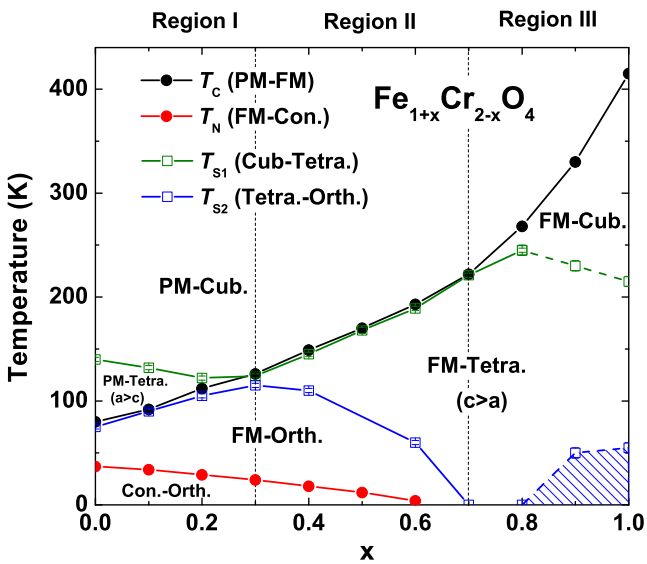

FIG. 8. (Color online) The temperature versus Fe content (x) phase diagram of $Fe_{1+x}Cr_{2-x}O_4$. T_C is the paramagnetic-to-collinear ferrimagnetic phase transition temperature(black lines and dots), T_N is the collinear-to-conical ferrimagnetic phase transition temperature(red lines and dots), T_{S_1} is the cubic-to-tetragonal lattice transition temperature(olive line with open squares), and T_{S_2} is the tetragonal-to-orthorhombic lattice transition temperature(blue line with open squares). The solid lines display the structural and magnetic transitions, while the dashed lines display the possible structural distortions.

$$H = -A(\tau_x Q_2 + \tau_z Q_3)\,, \qquad (2)$$

where τ is the Pauli matrix and A is the coupling constant.

As discussed by Öpik and Pryce,[51] the total of the orbital-lattice coupling in Eq.(2) and the Q_2 (Q_3) related harmonic potential energy can be minimized by an infinite number of distortions, however, the orbital degeneracy can be lifted by the anharmonic lattice potential term of the total potential energy,

$$V = \frac{1}{2}M\omega^2 Q^2 + A_3 Q^3 cos3\theta + \cdots\,, \qquad (3)$$

where Q and θ are the polar coordinations for $Q_2 - Q_3$ space. A_3 is the term describing the anharmonic effect on the tetragonal distortion. If $A_3 > 0$, the complex is compressed along the tetragonal axis; If $A_3 < 0$, the complex is elongated along the tetragonal axis.[34,51]

For the low Fe-doping FeO_4 tetrahedron ($x \leq 0.3$), the e_g orbital shape is deduced to be of $3d_{z^2}$ type in the paramagnetic phase, thus A_3 is positive and $a/c > 1$, as shown in Fig. 8. As more empty e_g Cr^{3+} ions are replaced by the half filled e_g Fe^{3+} ions, the Jahn-Teller distortion of Fe^{2+} ions becomes unstable and T_{S_1} decreases gradually.

As temperature decreases, the ferrimagnetic state is reached and the effect of spin-orbit coupling needs to be included in the total Hamiltonian. Although the first-order perturbation of spin-orbit coupling is absent, the second-order term $\lambda\mathbf{L}\cdot\mathbf{S}$ breaks the degeneracy of the two e_g orbitals and lowers the energy of the $3d_{x^2-y^2}$ relative to the $3d_{z^2}$ orbital.[34,51,52] The second-order perturbation of the Hamiltonian H_{SO} can be presented as,

$$H_{SO} = \frac{B}{6}((3S_z^2 - S^2)\tau_z - \sqrt{3}(S_x^2 - S_y^2)\tau_x)\,, \qquad (4)$$

where B is the energy difference between $3d_{x^2-y^2}$ and $3d_{z^2}$ states.

TABLE II. Refined atomic positions of $Fe_{1+x}Cr_{2-x}O_4$ (x=0.2, 0.3, 0.6, 0.8, and 1.0) from NPD data at 5 K.

	atoms	*site*	x	y	z
x =0.2	Fe(1)	8a	0.125	0.125	0.125
	Fe(2)	16d	0.5	0.5	0.5
	Cr	16d	0.5	0.5	0.5
	O	32e	0.261(2)	0.265(2)	0.259(2)
x =0.3	Fe(1)	8a	0.125	0.125	0.125
	Fe(2)	16d	0.5	0.5	0.5
	Cr	16d	0.5	0.5	0.5
	O	32e	0.262(2)	0.265(2)	0.258(2)
x =0.6	Fe(1)	8a	0.125	0.125	0.125
	Fe(2)	16d	0.5	0.5	0.5
	Cr	16d	0.5	0.5	0.5
	O	32e	0.263(2)	0.265(2)	0.260(2)
x =0.8	Fe(1)	4a	0.0	0.75	0.125
	Fe(2)	8d	0.0	0.0	0.5
	Cr	8d	0.0	0.0	0.5
	O	16h	0.0	0.020(2)	0.262(1)
x =1.0	Fe(1)	8a	0.125	0.125	0.125
	Fe(2)	16d	0.5	0.5	0.5
	Cr	16d	0.5	0.5	0.5
	O	32e	0.259(2)	0.259(2)	0.259(2)

Thus, the sign of A_3 is changed to negative to form the orthorhombic phase at low temperature, and T_C is above the associated structural transition temperature T_{S_2}.[34,51]

At the same time, the magnetic transition temperature could be roughly estimated by mean-field-theory,

$$3k_B T_C = z\sum_{i,j} J_{ij}\mathbf{S_i}\cdot\mathbf{S_j}\,, \qquad (5)$$

where z is the number of nearest neighbors, $\mathbf{S}$ and J_{ij} are the related moment and exchange energy, respectively.

Since the extra half-filled e_g electrons of the doped Fe^{3+} ions increase not only the interaction between A- and B-site ions (J_{AB}), but also the total moment of B-site ions($S_{Fe^{3+}/Cr^{3+}}$), T_C increases with the doping-amount of Fe^{3+} ions, which drives T_{S_2} to increase. Compared to the decreasing T_{S_1}, they meet at around $x = 0.3$. Hence, $x = 0.3$ is also the boundary of the two tetragonal phases with different c/a, Fig. 8.

As in the other spinel compounds with magnetic A^{2+} ions, $MnCr_2O_4$ and $CoCr_2O_4$, a conical magnetic state is also observed in the low Fe-doped $FeCr_2O_4$ at the lower temperature due to the geometrical magnetic frustration.[13–15,18,19] Furthermore, the transition temperature T_N decreases with Fe^{3+}-doping. Lyons et al.[16] had presented that the conical state is complicated and deduced the structure from a factor of u, which is closely related to the properties of both moments and interactions between the $A-$ and $B-$site cations, $4J_{BB}S_B/3J_{AB}S_A$. They presented that the conical state is stable as $8/9 \leq u \leq 1.298$. This factor is possibly related with the decreases of T_N. However, it is hard to obtain the u-value for $Fe_{1+x}Cr_{2-x}O_4$ quantitatively because of lack of information on the exchange energies, although S_B, J_{BB}, and J_{AB} are increasing with Fe-doping. Inelastic neutron scattering measurements using single crystal are needed to clarify the statement as MnV_2O_4.[53] Another possible reason would be that the extra Fe^{3+} on the $B-$site disturbs the homogeneous frustrated interactions and decreases T_N.

ii) $0.3 < x \leq 0.7$,

As in Region I ($x \leq 0.3$), the doped-Fe^{3+} ions occupy the B-site of the spinel with the normal spinel structure in Region II, $Fe^{2+}[Cr^{3+}_{2-x}Fe^{3+}_x]O_4$. Although the tetragonal-to-orthorhombic phase transition still follows the cubic-to-tetragonal transition, the lattice constant ratio, a/c, of the tetragonal phase is less than 1. In addition, the driving forces of the two structural transitions are the reverse of those in Region I, which means that the spin-orbital coupling effect on the Jahn-Teller distortion leads to the cubic-to-tetragonal transition, while the tetragonal-to-orthorhombic transition is due to the B-site disorders of Fe^{3+} and Cr^{3+} ions. Thus, T_{S_1} increases with Fe-doping, and T_{S_2} decreases to 0 as x approaches 0.7. For the magnetic ordering transitions, T_C accompanies the first structural distortion (T_{S_1}), which increases linearly with Fe-doping. The spin reorientation transition, occurring at T_N, continues to decrease and disappears at $x = 0.6$.

iii) $0.7 < x \leq 1.0$,

Unlike Region I and II, the doped-Fe^{3+} ions begin to occupy the A-site, and the Fe^{2+} ions move to the B-site of the spinel at $x \geq 0.7$, which makes the system very complicated, $Fe^{2+}_{1.7-x}Fe^{3+}_{x-0.7}[Cr^{3+}_{2-x}Fe^{3+}_{0.7}Fe^{2+}_{x-0.7}]O_4$. As presented in Fig. 8, T_C increases more sharply than the linear relationship in region II due to the electron hoping effect between A- and B-site Fe^{2+}/Fe^{3+} ions, which was confirmed by the reported Mössbauer measurement.[36,45]

The T_{S_1} continues the ascending trend for x up to 0.8, after which it disappears. Nevertheless, some structural distortions seem to persist up to the high-doping region ($0.8 \leq x \leq 1$) , as evidenced by the anomalies of the magnetic susceptibility measurements as shown in Fig. 2, as well as by the different width of the (004) Bragg peak between 20 and 300 K, as shown in Fig. 3(d). However, the magnetic ordering and structural distortion temperature are disconnected and the T_C rised steeply. If we still use T_{S_1} to label the temperature of the tetragonal distortion, it decreases due to the electron hopping effect on the orbitals of the Fe^{2+} and Fe^{3+} ions, as more Fe^{3+} ions are introduced in the system, indicated by the green dashed line in Fig. 8. Moreover, another structural distortion is observed at lower temperature, and it is suggested to be the orthorhombic/monoclinic distortion related to the extra Jahn-Teller active Fe^{2+} on the B-site, which is related to the t_{2g} orbital freedom found in inverse spinel Fe_3O_4.[54] T_{S_2} still describes this distortion and is presented as the shaded region in Fig. 8.

V. CONCLUSION

The structural and magnetic phase diagram of $Fe_{1+x}Cr_{2-x}O_4$ is investigated by means of magnetization, specific heat, x-ray and neutron scattering measurements. The substitution of Fe^{3+} for Cr^{3+} enhances the paramagnetic-to-collinear ferrimagnetic transition temperature T_C and reduces the collinear-to-conical ferrimagnetic transition temperature T_N, which is likely due to the complicated interactions between A- and B-site ions.

Systematic changes in the crystal structure with temperature and composition are observed. In the low Fe^{3+}-doped compound ($x \leq 0.7$), both cubic-to-tetragonal and tetragonal-to-orthorhombic transitions are driven by the Jahn-Teller distortion and the related spin-orbital couplings. At $x \leq 0.3$, the magnetic energy stabilizes the orthorhombic phase to increase T_{S_2}, while the disorder of the B-site ions(Fe^{3+}/Cr^{3+}) leads to the decreasing T_{S_1}; at $0.3 < x \leq 0.7$, the magnetic energy increases T_{S_1}, while the disorder of the B-site ions decreases T_{S_2}. In the high Fe^{3+}-doped compound ($x > 0.7$), a strong electron hoping mechanism between Fe^{2+} and Fe^{3+} ions lead to the orbital-active Fe^{2+} ions occupying both A- and B-site of the spinel, and the related e_g and t_{2g} orbital effects are observed, which results in the temperature dependence of the lattice distortions.

ACKNOWLEDGEMENT

The research at the High Flux Isotope Reactor, Oak Ridge National Laboratory was sponsored by the Scientific User Facilities Division (J.M., M.M., C.D.D.C., O.G., S.C., W.T., A.A.A., S.X.C.) and Center for Nanophase Materials Sciences (A.R.), Office of Basic Energy Sciences, US Department of Energy. R.S. and H.D.Z. thanks for the support from JDRD program of University of Tennessee. Work at FSU is supported in part by NSF-DMR 1005293, and carried out at the National High Magnetic Field Laboratory, supported by the NSF, the DOE, and the State of Florida.

[1] S.-H. Lee, C. Broholm, W. Ratcliff, G. Gasparovic, Q. Huang, T. H. Kim, and S.-W. Cheong, Nature **418**, 856-858 (2002).
[2] S. T. Bramwell, and M. J. P. Gingras, Science **294**, 1495-1501 (2001).
[3] A. P. Ramirez, *Handbook of Magnetic Materials* (Elsevier, Amsterdam, 2001), vol. 13, pp. 423-520.
[4] Y. Kino and B. Lüthi, Solid State Commun. **9**, 805 (1971).
[5] S.-H. Lee, C. Broholm, T. H. Kim, W. Ratcliff II, and S.-W. Cheong, Phys. Rev. Lett. **84**, 3718 (2000).
[6] A. B. Sushkov, O. Tchernyshyov, W. Ratcliff, S. W. Cheong, and H. D. Drew, Phys. Rev. Lett. **94**, 137202 (2005).
[7] M. C. Kemei, P. T. Barton, S. L. Moffitt, M. W. Gaultois, J. A. Kurzman, R. Seshadri, M. R Suchomel, and Y.-II Kim, J. Phys.: Condens. Matter **25**, 326001 (2013).
[8] S.-H. Lee, H. Takagi, D. Louca, M. Matsuda, S. Ji, H. Ueda, Y. Ueda, T. Katsufuji, J.-H. Chung, S. Park, S.-W. Cheong, and C. Broholm, J. Phys. Soc. Jpn. **79**, 011004 (2010).
[9] H. Mamiya, M. Onoda, T. Furubayashi, J. Tang, and I. Nakatani, J. Appl. Phys. **81**, 5289 (1997).
[10] J.-H. Chung, M. Matsuda, S.-H. Lee, K. Kakurai, H. Ueda, T. J. Sato, H. Takagi, K.-P. Hong, and S. Park, Phys. Rev. Lett. **95**, 247204 (2005).
[11] H. Ueda, H. Mitamura, T. Goto, and Y. Ueda, Phys. Rev. B **73**, 094415 (2006).
[12] M. Matsuda, H. Ueda, A. Kikkawa, Y. Tanaka, K. Katsumata, Y. Narumi, T. Inami, Y. Ueda, and S.-H. Lee, Nat. Phys. **3**, 397-400 (2007).
[13] J. M. Hastings, and L. M. Corliss, Phys. Rev. **126**, 556 (1962).
[14] K. Tomiyasu, J. Fukunaga, and H. Suzuki, Phys. Rev. B **70**, 214434 (2004).
[15] C. Ederer, and M. Komelj, Phys. Rev. B **76**, 064409 (2007).
[16] D. H. Lyons, T. A. Kaplan, K. Dwight, and N. Menyuk, Phys. Rev. **126**, 540 (1962).
[17] V. Kocsis, S. Bordács, D. Varjas, K. Penc, A. Abouelsayed, C. A. Kuntscher, K. Ohgushi, Y. Tokura, and I. Kézsmárki, Phys. Rev. B **87**, 064416 (2013).
[18] N. Menyuk, K. Dwight, and A. Wold, J. Phys. (Paris) **25**, 528 (1964).
[19] R. Plumier, J. Appl. Phys. **39**, 556 (1968).
[20] K. Singh, A. Maignan, C. Simon, and C. Martin, Appl. Phys. Lett. **99**, 172903 (2011).
[21] S. Bordács, D. Varjas, I. Kézsmárki, G. Mihály, L. Baldassarre, A. Abouelsayed, C. A. Kuntscher, K. Ohgushi, and Y. Tokura, Phys. Rev. Lett. **103**, 077205 (2009).
[22] K. Ohgushi,Y.Okimoto, T. Ogasawara, S. Miyasaka, andY. Tokura, J. Phys. Soc. Jpn. **77**, 034713 (2008).
[23] K. Tomiyasu, H. Hiraka, K. Ohoyama, and K. Yamada, J. Phys. Soc. Jpn. **77**, 124703 (2008).
[24] M. Tanaka, T. Tokoro, and Y. Aiyama, J. Phys. Soc. Jpn. **21**, 262 (1966).
[25] G. Shirane, D. E. Cox, and S. J. Pickard, J. Appl. Phys. **35**, 954 (1964).
[26] K. Tomiyasu, and I. Kagomiya, J. Phys. Soc. Jpn. **73**, 2539 (2004).
[27] M. R. Suchomel, D. P. Shoemaker, Lynn Ribaud, M. C. Kemei, and R. Seshadri, Phys. Rev. B **86**, 054406 (2012).
[28] E. Prince, Acta Crystallogr. 10, 554 (1957).
[29] E. Jo, B. Kang, C. Kim, S. Kwon, and S. Lee, Phys. Rev. B **88**, 094417 (2013).
[30] Y. Yamasaki, S. Miyasaka, Y. Kaneko, J.-P. He, T. Arima, and Y. Tokura, Phys. Rev. Lett. **96**, 207204 (2006).
[31] N. Mufti, A. A. Nugroho, G. R. Blake, and T. T.M. Palstra, J. Phys.: Condens. Matter **22**, 075902 (2010).
[32] M. Kataoka and J. Kanamori, J. Phys. Soc. Jpn. **32**, 113 (1972).
[33] H. Katsura, N. Nagaosa, and A. V. Balatsky, Phys. Rev. Lett. **95**, 057205 (2005).
[34] S. Ohtani, Y. Watanabe, M. Saito, N. Abe, K. Taniguchi, H. Sagayama, T. Arima, M. Watanabe and Y. Noda, J. Phys.: Condens. Matter **22**, 176003 (2010).
[35] H. Sagayama, S. Ohtani, M. Saito, N. Abe, K. Taniguchi, and T. Arima, Appl. Phys. Lett. **99**, 082506 (2011).
[36] M. Robbins, G. K. Wertheim, R. C. Sherwood, and D. N. E. Buchanan, J. Phys. Chem. Solids **32**, 717 (1971).
[37] H. J. Yearian, J. M. Kortright, and R. H. Langenheim, J. Chem. Phys. **22**, 1196 (1954).
[38] E. J. W. Verwey, and E. L. Heilmann, J. Chem. Phys. **15**, 174 (1947).
[39] A. Ramdani, C. Gleitzer, G. Gavoille, A. K. Cheetham, and J. B. Goodenough, J. Solid State Chem. **60**, 269 (1985).
[40] A. Kyono, S. A. Gramsch, T. Yamanaka, D. Ikuta, M. Ahart, B. O. Mysen, H. -K. Mao, and R. J. Hemley, Phys. Chem. Miner. **39**, 131 (2012).
[41] H. J. Levinstein, M. Robbins, and C. Capio, Mater. Res. Bull. **7**, 27 (1972).
[42] K. Kose, and S. Iida, J. Appl. Phys. **55**, 2321 (1984).
[43] M. H. Francombe, J. Phys. Chem. Solids **3**, 37 (1957).
[44] H. N. Ok, L. S. Pan, and B. J. Evans, Phys. Rev. B **17**, 85 (1978).
[45] M. Quintiliani, G. B. Andreozzi, and H. Skogby, Periodico di Mineralogia, **80**, 39-55 (2011).
[46] J. Rodriguez-Carvajal, Physica B **192**, 55 (1993).
[47] G. J. MacDougall, V. O. Garlea, A. A. Aczel, H. D. Zhou, and S.E. Nagler, Phys. Rev. B **86**, 060414 (2012).
[48] J. D. Lee, and D. Schroeer, J. Phys. Chem. Solids **37**, 739 (1976).
[49] N. Liu, K. H. Zhao, X. L. Shi, and L. W. Zhang, J. Appl. Phys. **111**, 124112 (2012).
[50] J. H. Van Vleck, J. Chem. Phys. **7**, 72 (1939).
[51] U. Öpik and M. H. L. Pryce, Proc. R. Soc. A **238**, 425 (1957).
[52] J. Kanamori, J. Appl. Phys. **31**, S14 (1960).
[53] V.O. Garlea, R. Jin, D. Mandrus, B. Roessli, Q. Huang, M. Miller, A. J. Schultz, S.E. Nagler, Phys. Rev. Lett. **100**, 066404 (2008); J.-H. Chung, Y.-S. Song, J.-H. Kim, T. Suzuki, T. Katsufuji, M. Matsuda, and S.-H. Lee, Phys. Rev. B **88**, 094430 (2013).
[54] J. P. Wright, J. P. Attfield, P. G. Radaelli, Phys. Rev. B **66**, 214422 (2002)